Electrochemistry
The Electrochemical Society of Japan
Received: September 6, 2023
Accepted: December 28, 2023
Published online: January 12, 2024
Issued: February 15, 2024
https://doi.org/10.5796/electrochemistry.23-00087
https://doi.org/10.50892/data.electrochemistry.24980718
Article
Electrochemistry, 92(2), 027003 (2024)

Ether Molecule Decomposition on MgM_2O_4 (M = Mn, Fe, Co) Spinel Surface: A First-principles Study

Tomoaki KANEKO,[a,e,*] Yui FUJIHARA,[b,§] Toshihiko MANDAI,[c,§] Hiroaki KOBAYASHI,[d,§] and Keitaro SODEYAMA[e,*]

[a] Department of Computational Science and Technology, Research Organization for Information Science and Technology, 1-18-16 Hamamatsucho, Minato, Tokyo 105-0013, Japan
[b] Energy Transformation Research Laboratory, Central Research Institute of Electric Power Industry, 2-6-1 Nagasaka, Yokosuka 240-0196, Japan
[c] Center for Advanced Battery Collaboration, Center for Green Research on Energy and Environmental Materials, National Institute for Materials Science (NIMS), 1-1 Namiki, Tsukuba 305-0044, Japan
[d] Department of Chemistry, Faculty of Science, Hokkaido University, Kita 10, Nishi 8, Kita-ku, Sapporo 060-0810, Japan
[e] Data-driven Materials Research Field, Center for Basic Research on Materials, National Institute for Materials Science (NIMS), 1-1 Namiki, Tsukuba 305-0044, Japan

* Corresponding authors: kaneko.tomoaki@rist.or.jp (T. K.), SODEYAMA.Keitaro@nims.go.jp (K. S.)

ABSTRACT

The transition between MgM_2O_4 (M = Mn, Fe, Co) spinels (SPs) and $MgMO_2$ rock salts (RS) has attracted considerable interest for cathode reactions in future magnesium battery applications. To improve the cycling performance, one should suppress the consumption of solvent molecules. In this study, we investigated ether solvent decomposition on MgM_2O_4 SP and $MgMO_2$ RS surfaces using first-principles calculations. We found that the C–H bond dissociation of ether molecules on the SP surface was exothermic, while the C–H bond dissociation on RS and C–O bond dissociation on both SP and RS surfaces were endothermic, irrespective of the transition metal element. The products of C–H dissociation reactions at the SP surfaces have occupied states originating from SP surfaces inside the bandgap. As the SP surface is destabilized by C–H dissociation, the electrons at this level can be extracted as an oxidative current.

Keywords : First-principles Calculations, Mg-battery, Solvent Decomposition, Mg-spinel

1. Introduction

The demand for rechargeable batteries with high energy densities has increased because of the widespread use of portable electronic devices and vehicles. Mg batteries have attracted significant interest for their future high rechargeability[1] because of the high specific capacity of magnesium metal anodes (2200 mAh g^{-1}) compared to the graphite anodes (370 mAh g^{-1}) used in conventional lithium-ion batteries. MgM_2O_4 (M = Mn, Fe, Co)-based spinels (SP) are considered promising candidates for use as cathode materials in magnesium batteries. During the discharging process, the SP transforms into the $MgMO_2$ rock salt (RS) phase:

$$MgM_2O_4 + Mg^{2+} + 2e^- \rightleftharpoons 2MgMO_2. \quad (1)$$

Although Mg batteries with an SP cathode exhibit a high potential (2–3 V vs. Mg^{2+}/Mg) and high capacities (260–270 mAh g^{-1}), poor reversibility and slow kinetics are critical problems for practical applications.[1,2] The consumption of solvent or anion molecules during cycling is considered a critical problem in the cycle performance. The purpose of this study was to discuss and gain further insight into the decomposition of solvent molecules at cathode surfaces using first-principles calculations.

For Mg batteries with SP cathodes, the oxidative decomposition of the solvent is an important issue for practical applications. Owing to the undesired decomposition of electrolytes at the cathode–electrolyte interface during charging, the deliverable capacity decreases drastically upon cycling. The adsorption and subsequent decomposition of ether at the [cathode | electrolyte] interface would impede intercalation/deintercalation of Mg^{2+} into/from the cathode due to the large diffusion barrier of decomposition products generated at the interface. This undesired side reaction can consequently lead to continuous decrease of the deliverable capacities with cycling. To address these critical issues, certain inorganic and organic ionic liquid-based electrolytes have been developed and applied to Mg batteries; however, these oxidatively stable electrolytes are less compatible with Mg metal anodes.[3,4]

Recently, the oxidation potentials of ether solvent decomposition for MgM_2O_4 in Mg batteries were determined experimentally and computationally.[5,6] Han et al. observed the oxidation decomposition of ether-based electrolytes on SP cathodes at a lower oxidation potential than their potential anodic limits and suggested the specific catalytic activity of SP cathodes against ether solvents.[5,6] They also reported the highest oxidation potential of ether solvents when $MgFe_2O_4$ was used as a cathode.[5,6] The origin of such transition-element-dependent oxidation potentials of ether solvents can be explained by the electronic structures of the SP cathode and differences in the HOMO energy levels between the solvent ethers and SP cathode surfaces. However, the detailed decomposition mechanism and the decomposition behavior on RS cathodes remain unclear.

§ECSJ Active Member
T. Kaneko orcid.org/0000-0002-5296-7403
Y. Fujihara orcid.org/0000-0002-4842-5740
T. Mandai orcid.org/0000-0002-2403-7794
H. Kobayashi orcid.org/0000-0001-6705-9515
K. Sodeyama orcid.org/0000-0002-9228-0729

In contrast, theoretical studies on solvent decomposition on the cathode surfaces of the Mg battery is limited. Han et al. discussed the origin of oxidative decomposition by the electronic structures of the SP surfaces.[5,6] For the cathode materials of Li-ion batteries, solvent molecule decomposition on the cathode surface has been intensively investigated by several authors.[7–29] However, most studies have been conducted on ethylene carbonate (EC) and related carbonate molecules, such as fluoroethylene carbonate and diethyl carbonate, while only quite recent report handles the decomposition of ether molecules.[29] Another quite recent work by Zhou et al. reports the decomposition of 1,2-dimethoxyethane on the SP surface and the decomposition reaction on SP surface is mainly determined by the catalytic chemistry of SP surface.[30] Therefore, the understanding of oxidative decomposition at the SP surface is still limited.

In this study, we performed first-principles calculations to investigate the origin of oxidative decomposition at the cathodes of Mg batteries.

2. Computational Details

In this study, we employed the quantum espresso code,[34] which is a first-principles calculation code based on density functional theory with a plane-wave basis set. The generalized gradient approximation (GGA)[35] and ultrasoft pseudopotentials were used.[36,37] In our calculations, the semicore states of 2s and 2p orbitals of Mg and 3s and 3p orbitals of Mn, Fe, and Co were treated as valence electrons. The DFT-D3 dispersion correction was considered.[38] For *d*-orbitals of Mn, Fe, and Co, an isotropic model of DFT+U was adopted.[39] The U_{eff} values were 5.0, 5.0, and 6.0 eV for Mn, Fe, and Co, respectively, which are typical values, as discussed in our previous paper.[40] The cutoff energies of the plane-wave basis set and the charge density were selected to be 35 and 315 Ry, respectively. For the calculations of primitive cells, we used a special *k*-sampling of $2 \times 2 \times 2$. The lattice constants of $MgFe_2O_4$ (SP-MFO) and $MgCo_2O_4$ (SP-MCO) were determined by minimizing the total energy. To optimize the lattice constant of SP $MgMn_2O_4$ (SP-MMO) using a stress tensor, cutoff energies of the plane wave basis set and charge densities of 55 and 495 Ry, respectively, were employed because SP-MMO belongs to the tetragonal lattice system owing to the strong Jahn-Teller effect in Mn^{3+}. We assumed antiferromagnetic ordering along the [110] direction, alternating between spins up and down.[41] For SP-MCO, a low-spin state is adopted for Co^{3+} because it is more stable than the high-spin state.

The RS phases of $MgMnO_2$ (RS-MMO), $MgFeO_2$ (RS-MFO), and $MgCoO_2$ (RS-MCO) are also calculated. For simplicity, we assumed that the transition metal atoms reside at the same site in SP and that the Mg atoms occupy the 16c site of the RS phase. As summarized in Table 1, the optimized lattice constants agree well with the experimental values, except for a few % changes. Then, the voltage of with Mg metal anode is defined as

Table 1. Results of bulk materials.

	Mn	Fe	Co
a_{SP}, c_{SP} (Å)	8.227, 9.575	8.576	8.166
Exp.	8.099, 9.284[a]	8.397[b]	8.138[c]
Diff.	1.5 %, 3.1 %	2.1 %	3.4 %
a_{RS} (Å)	8.798	8.660	8.567
Exp.	8.672[d]		8.503[c]
Diff.	1.5 %		7.5 %
$V_{\mathrm{Mg/Mg^{2+}}}$ (V)	2.20	1.86	2.75
Exp.	2.3[c]	2.2[c]	2.9[c]

a: Ref. 31, *b*: Ref. 32, *c*: Ref. 3, *d*: Ref. 33.

$$V_{\mathrm{Mg/Mg^{2+}}} = -\frac{1}{2e}[2E_{\mathrm{Mg}MO_2} - E_{\mathrm{Mg}M_2O_4} - E_{\mathrm{Mg}}], \quad (2)$$

where $E_{\mathrm{Mg}MO_2}$, $E_{\mathrm{Mg}M_2O_4}$, E_{Mg} are the total energies per formula units for SP, RS, and Mg in hcp lattice, respectively. The obtained $V_{\mathrm{Mg/Mg^{2+}}}$ values were 2.20 for Mn, 1.86 for Fe, and 2.75 for Co. These results agree well with the experimental results reported in Ref. 3, i.e., 2.3 for Mn, 2.2 for Fe, and 2.9 for Co, and our previous calculations without vdW correction.[40]

We considered the (001) cleaved slab models of SP and RS surfaces, with the thickness of the slab model as a single primitive size. For the SP surface, we used the RS-like reconstruction surface model previously reported in Ref. 40. The surface slab models are charge neutral. For surface calculations, we used special k-sampling of $2 \times 2 \times 1$. To remove the spurious interactions between periodic images, an effective screening medium was employed[42] with a vacuum layer thicker than 10 Å on both sides of the slab. For the projected density of states (PDOS) calculations, we used Γ point centered $4 \times 4 \times 1$ k-sampling.

In the experiments, glyme molecules such as tri-glyme (G3) and tetra-glyme (G4) were used as solvents. However, such glyme molecules are excessively long to simulate, that is, their adsorption structures are complicated, and the number of possible reactions increases dramatically. As mentioned in the Introduction, there are only a few reports of theoretical studies on ether molecule decomposition on the surface of the cathode of Mg batteries. Therefore, we consider the simplest ether molecule, dimethylether (Me_2O), in the primary stage of this study. We define the adsorption energy (E_{ads}) as follows:

$$E_{\mathrm{ads}} = E_{\mathrm{surf+ads}} - E_{\mathrm{surf}} - E_{\mathrm{mol}}, \quad (3)$$

where $E_{\mathrm{surf+ads}}$, E_{surf}, and E_{mol} denote the total energies of the surface with the adsorbate, surface, and Me_2O molecules, respectively. Bader charge analysis was performed using bader code.[43–46] The results of the Bader charge are summarized in the Supporting Information.

The O atoms in Me_2O were placed at the Mg and *M* (Mn, Fe, Co) atom sites on the SP or RS surfaces. We consider the following reactions, referred to as cut-1 and cut-2:

$$Me_2O \rightarrow CH_3O + CH_3 \quad \text{(cut-1)}, \quad (4)$$

and

$$Me_2O \rightarrow CH_3OCH_2 + H \quad \text{(cut-2)}. \quad (5)$$

The CH_3 radial and H ions were placed on the surface of O atoms. Hereafter, the oxygen atom of Me_2O is referred to as O_{Me_2O}. The notations O_{Me_2O}@Mg and O_{Me_2O}@*M* represent the adsorption sites on O_{Me_2O}. We define the reaction energy by the change in the adsorption energy. In this paper, we neglected the solvation effect of the molecule. The adsorption energy may change by considering the solvation effect. On the other hand, the effect of solvation on the reaction energy would be much smaller than that of adsorption energy, since the reactant and product are adsorbed on the surfaces.

3. Results and Discussion

First, we discuss the structural properties and energetics of Me_2O decomposition. The calculated adsorption energies are summarized in Table 2. In this table, O_{Me_2O}@Mg and O_{Me_2O}@*M* denote the adsorption sites of Me_2O. In Fig. 1a, ball-stick models of adsorbates on SP-MCO for the O@*M* case are shown. The other results are summarized in the Supporting Information.

For the SP surfaces, Me_2O was preferentially adsorbed at the Mg site for SP-MMO, whereas it was preferentially adsorbed at the transition metal site for SP-MFO and SP-MCO. The calculated Mg–O and *M*–O interatomic distances for Me_2O adsorption are

Table 2. Me_2O adsorption energy (E_{ads}) on the SP and RS surfaces.

	SP-MMO	SP-MFO	SP-MCO	RS-MMO	RS-MFO	RS-MCO
Me_2O, O_{Me_2O}@Mg	−0.691	−0.745	−0.868	−0.647	−0.695	−0.657
Me_2O, O_{Me_2O}@*M*	−0.463	−0.814	−1.297	−0.528	−0.609	−0.514
cut-1, O_{Me_2O}@Mg	+0.664	+0.543	+0.331	+0.427	+0.538	+0.544
cut-1, O_{Me_2O}@*M*	+0.270	−0.649	−0.041	+0.340	+0.330	+0.408
cut-2, O_{Me_2O}@Mg	−1.233	−1.731	−2.182	+0.535	+0.720	+0.522
cut-2, O_{Me_2O}@*M*	−1.357	−2.009	−3.942	+0.578	+0.695	+0.585

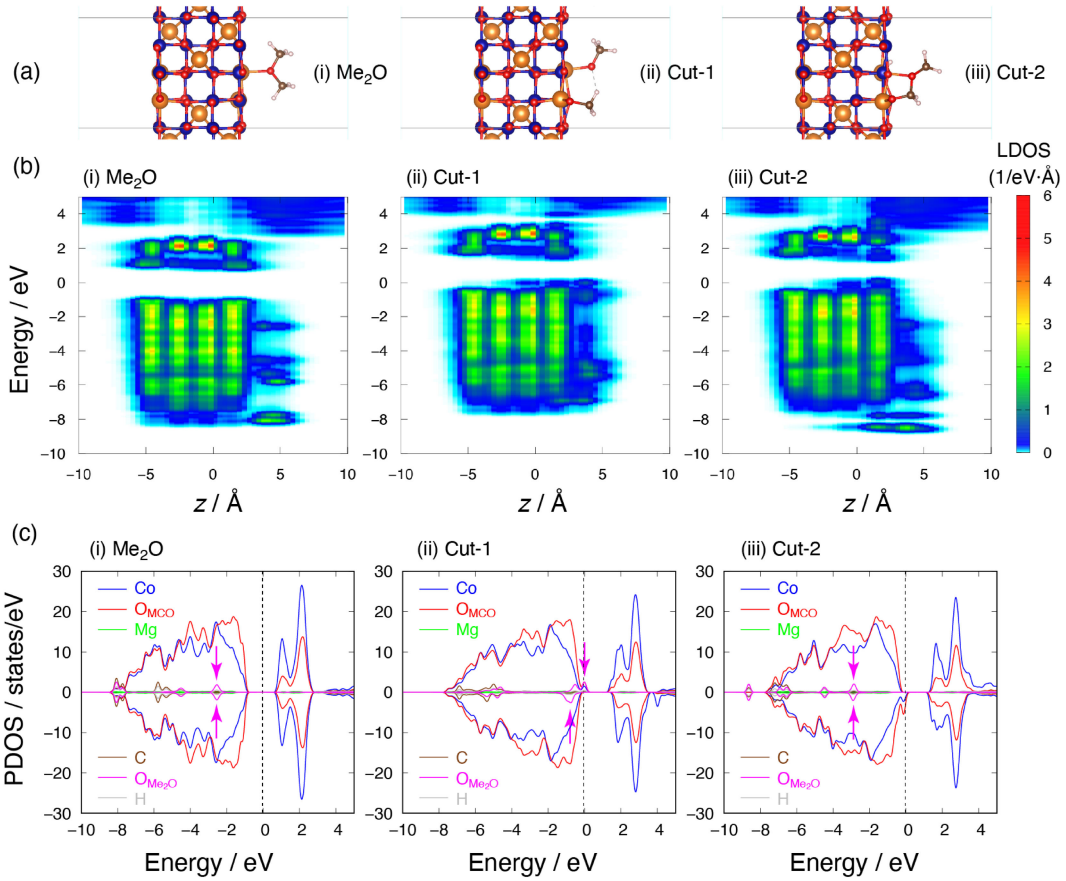

Figure 1. (a) Optimized structures of (i) pristine Me_2O, (ii) cut-1, and (iii) cut-2 for SP-MCO and O_{Me_2O}@Mg. (b) Local density of states of (i) pristine Me_2O, (ii) cut-1, and (iii) cut-2 for SP-MCO and O_{Me_2O}@Mg. (c) PDOS of (i) pristine Me_2O, (ii) cut-1, and (iii) cut-2 for SP-MCO and O_{Me_2O}@Mg.

summarized in the Supporting Information. The different trends in the adsorption sites on SP-MMO from SP-MFO or SP-MCO are caused by the strong Jahn–Teller effect in SP-MMO, that is, the Mn–O interatomic distance is much longer than that in SP-MFO or SP-MCO. Such an electronic configuration of the surface Mn ion plays an important role in the energetics of adsorbates.

However, for the adsorbates of Cut-1 and Cut-2, the adsorption energies for O_{Me_2O}@*M* were lower than those for O_{Me_2O}@Mg. In the Cut-1 structure, the H atom in the methyl group forms a hydrogen bond with the O in Me_2O for SP-MCO. We observed the same trend for the other transition metal elements, as shown in the Supporting Information. In the Cut-2 structure, the dangling bond at the C atom was passivated by the topmost O atom of SP-MCO. As shown in the Supporting Information, this behavior is the same as that of other *M* elements, except for SP-MMO, O_{Me_2O}, and *M*. Interestingly, the adsorbate was stabilized by disconnecting the bond between O_{Me_2O} and *M* in Cut-2 at O_{Me_2O}@*M* of SP-MMO case.

We also performed a Bader charge analysis, and the results are provided in the Supporting Information. The number of valence electrons in Me_2O was 20. The total Bader charge of Me_2O was unchanged for pristine Me_2O and for the cut-1 reaction. However, the total Bader charge associated with adsorbate atoms decreases (18.17–18.70) by the cut-2 reaction. The Bader charge of the H atom for Cut-2 is summarized in the Supporting Information. Because the Bader charge of the surface H atom is much smaller than unity, the Cut-2 reaction can be understood as deprotonation instead of dehydrogenation.

Next, we consider the RS surface. For RS surfaces, Me_2O preferentially adsorbs at the Mg site, irrespective of the transition metal element. The adsorption energies become smaller for Cut-1 and O_{Me_2O}@*M* than for O_{Me_2O}@Mg, whereas the adsorption energies decrease to only a few tens meV difference for Cut-2. In Fig. 2a, ball-stick models of adsorbates on RS-MCO for O@*M* cases are shown. The results for the others are provided in the Supporting Information. The characteristics on structures of the Me_2O adsorption and Cut-1 are similar to those of the SP-surface cases. For Me_2O adsorption, the difference in the interatomic distances between O_{Me_2O} and the adsorption sites is much smaller

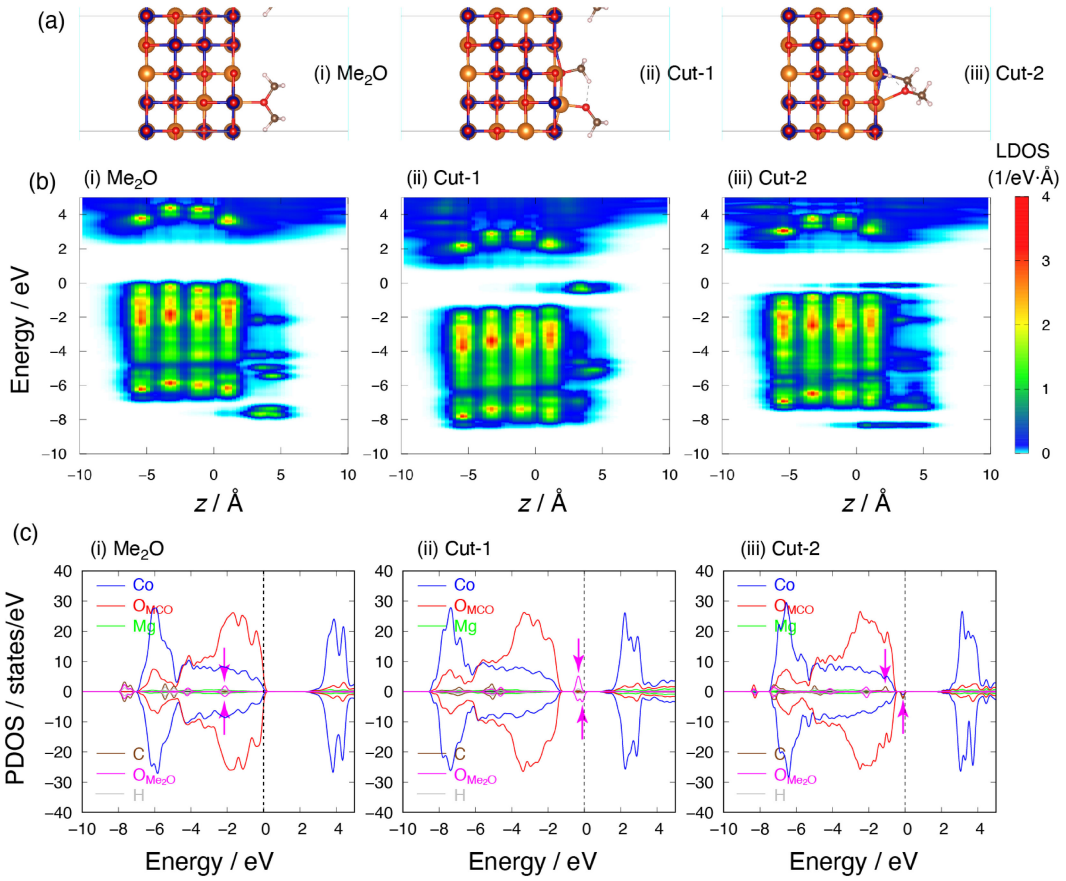

Figure 2. (a) Optimized structures of (i) pristine Me_2O, (ii) cut-1, and (iii) cut-2 for RS-MCO and O_{Me_2O}@Mg. (b) Local density of states of (i) pristine Me_2O, (ii) cut-1, and (iii) cut-2 for RS-MCO and O_{Me_2O}@Mg. (c) PDOS of (i) pristine Me_2O, (ii) cut-1, and (iii) cut-2 for RS-MCO and O_{Me_2O}@Mg.

Table 3. Reaction energy of Me_2O decomposition on SP and RS.

	SP-MMO	SP-MFO	SP-MCO	RS-MMO	RS-MFO	RS-MCO
cut-1, O_{Me_2O}@Mg	+1.354	+1.288	+1.199	+1.074	+1.233	+1.200
cut-1, O_{Me_2O}@*M*	+0.732	+0.165	+1.256	+0.868	+0.939	+0.922
cut-2, O_{Me_2O}@Mg	−0.543	−0.986	−1.315	+1.181	+1.415	+1.179
cut-2, O_{Me_2O}@*M*	−0.894	−1.195	−2.645	+1.111	+1.304	+1.099

than that in the SP-MMO case because of the absence of a strong Jahn–Teller effect. For Cut-2, the dangling bond at the C atom was passivated by the surface transition metal atom, whereas the dangling bond was passivated by the O atom on the SP surface.

For the Bader charge of the RS case, the total Bader charge was close to that of the isolated Me_2O molecule. However, the total Bader charge for cut-2 was much closer to that of the isolated Me_2O molecule. Because the Bader charge of the surface H is much smaller than that of the isolated molecule, the cut-2 reaction is deprotonation instead of dehydrogenation, similar to the SP-surface case. Then, an excess of electrons accumulated at the C atoms, which were connected to the surface H atoms (see Table S5). Consequently, the C atoms were anionic and passivated by the surface *M* atoms on the RS surface, whereas the C atoms were passivated by surface O on the SP surface. The M^{3+} ions receive an electron from a molecule on the SP surface, whereas the M^{2+} ions are difficult to reduce.

Next, we discuss the energies of the decomposition reactions. The calculated reaction energies are listed in Table 3. Here, the reaction energy is defined as the difference in the total energy, that is, the reaction is exothermic when the reaction energy is negative. For the SP surfaces, the reaction energy was negative for the Cut-2 reaction, irrespective of the adsorption site and transition metal, whereas the reaction energy of the Cut-1 reaction was positive. Because the reaction energy of the Cut-2 reaction becomes significantly more negative for O_{Me_2O}@*M* than for O_{Me_2O}@Mg, the Cut-2 reaction should occur at the *M* site. For the RS surfaces, on the other hand, the reaction energies are positive for both Cut-1 and Cut-2 reactions, that is, the reactions are endothermic.

We briefly mention the use of DFT+*U* calculations in the Results Section. The parameter *U* is used to enlarge the electronic correlation at the 3*d*-orbital, which is underestimated in DFT and GGA. The bandgap of transition metal oxides can be improved using appropriate *U* values. As mentioned in our previous study, the calculated $V_{Mg/Mg^{2+}}$ depends on U_{eff}. A quantitative comparison of the results, such as the reaction energies, between different SPs might be difficult. Therefore, we will not discuss a comparison of the transition metal element differences.

The decomposition of solvent molecules on cathode surfaces has been investigated by several researchers.[7–28] Most calculations

consider the ring-opening reactions of EC at the surface of the cathode materials of Li-ion batteries. Leung performed DFT-MD simulations of EC adsorbed onto a partially delithiated SP $Li_{0.6}Mn_2O_4$ surface.[7,10] The ring-opening reaction of EC and proton transfer from the product of the ring-opening reaction to the surface were observed. Proton transfer is a two-electron oxidative reaction triggered by the preceding ring-opening reaction. For the EC decomposition on SP $Li_{0.67}Mn_2O_4(111)$ surface, in contrast, the deprotonation occurs before the ring-opening reaction. In this case, the decomposition reaction is exothermic, whereas deprotonation is endothermic. Therefore, the results seem to be sensitive to the surface orientation.

Giordano et al. reported C–H bond dissociation of EC on layered type $Li_xMO_2(10\bar{1}4)$ and $MO(100)$ surfaces.[24,27] They showed that the C–H bond dissociation is exothermic for $Li_xMO_2(10\bar{1}4)$, whereas the reactions become endothermic for $MO(100)$. Our results are in good agreement with these results, although the cathode material and solvent molecules are different. Okuno et al. reported the decomposition of EC on $LiNi_{0.5}Mn_{1.5}O_4$ surface.[11] They found that the C–H dissociation reaction of pristine EC on partially delithiated $LiNi_{0.5}Mn_{1.5}O_4$ is sensitive to the H adsorption site of O, that is, the reaction is exothermic for a two-coordinated surface O and endothermic for a three-coordinated surface O. In our study, there were no two-coordinated surfaces O because we used a reconstructed surface. Therefore, the Cut-2 reaction becomes more exothermic when the SP surface is partially demagnethiated SP.

Next, we discuss electronic structures. The calculated PDOS of SP-MCO and RS-MCO with O_{Me_2O}@Mg are shown in Figs. 1c and 2c, respectively. In Figs. 1c and 2c, the up- and down-spin components of PDOS are presented in the top and bottom halves of each panel, respectively. The upward and downward arrows represent the up- and down-spin components of the highest occupied level in the solvent, respectively. In these figures, the energy was measured using Fermi energy. The results for the other SP and RS are summarized in the Supporting Information.

For SP-MCO surfaces, the HOMO level of Me_2O is 2.03 eV below the valence band top of SP-MCO as shown in Fig. 2b–(i). The positions of the HOMO levels of Me_2O measured from SP and RS surfaces are summarized in the Supporting Information. The range of the HOMO level position, measured from the top of the surface valence band, was 1.4–2.0 eV. For the Cut-1 model, the adsorbate levels appeared in the gap of SP-MCO as shown in Fig. 1c–(ii). This behavior was also observed for the other SP surfaces. In contrast, for the Cut-2 model, the levels originating from SP-MCO can be found in the gap of SP-MCO, and the HOMO levels of adsorbates are located outside the SP-MCO gap. This result is consistent with the decrease in the total Bader charge of Me_2O for the Cut-2 on SP. Notably, these trends are the same irrespective of the transition metal element and the adsorption site of O_{Me_2O}.

For the RS-MCO surface, the HOMO is 1.89 eV below the valence band top of RS-MCO. The range of HOMO levels measured from the valence band top is 1.9–2.7 eV, suggesting that the adsorbates are harder to oxidize compared with SP surfaces. For both the Cut-1 and Cut-2 models, adsorbate-related levels were observed inside the bandgap of RS-MCO. For the other RS surfaces, such adsorbate-related levels appeared inside the band gap or at the energetically similar position of the top of the valence band for Cut-1 and Cut-2, as summarized in the Supporting Information.

Next, we considered the mechanism of oxidative solvent decomposition at the cathode surface. Because the Cut-2 reactions on SP surfaces are exothermic irrespective of *M* element, we focused on the Cut-2 reaction, which is a unique candidate for oxidative decomposition. As discussed, the occupied states originating from SP surfaces appear just above the top of the valence band for the Cut-2 reaction, owing to the charge transfer from the adsorbate to SP. Notably, these occupied states are easier to oxidize than other states on the SP surface, which could be the origin of the oxidative current. Electrons and Mg ions were extracted from the cathode for oxidative decomposition at the cathode surface. Therefore, the partially demagnethiated SP surfaces are more likely to undergo decomposition.

Giordano et al. reported that the decomposition reaction becomes energetically favorable on the oxide surface with the transition metal element from left to right in the periodic table.[24,27] Although we can observe similar trends for the Cut-2 reaction, these results are sensitive to the magnitude of *U* parameters. If we are to make such conclusions, we need to check the *U* dependence of the reaction energy, which is beyond the scope of the present study. Giordano et al. also reported that the decomposition reaction becomes energetically favorable by increasing transition metal valence in the oxide, where a higher degree of EC dissociation was found as the Fermi level was lowered into the oxide O 2p band.

Next, we discuss the correspondence between the results, experiments, and other theories. Quite recently, Han et al. examined the oxidation potentials (E_{ox}) of the cyclic voltammograms of Mg batteries.[6] In their experiments, 0.5 mol dm^{-3} [Mg(G4)][TFSA]$_2$/[Pry1,3][TFSA] electrolytes at 100 °C were employed, where TFSA and Pry1,3 denote bis(trifluoromethanesulfonyl)amide and *N*-methyl-*N*-propylpyrrolidinium, respectively. The obtained E_{ox} are 3.05, 3.33, and 3.20 eV for SP-MMO, SP-MFO, and SP-MCO, respectively, that is, the oxidative decomposition is much suppressed for the SP-MFO cathode.[6]

To understand the experimental results, the electronic structures of the pristine $MgM_2O_4(100)$ (M = Mn, Fe, Co) surfaces were investigated.[6] In their discussion, the position of the top of the valence band of SP oxide measured from the vacuum level was used. The obtained levels of the valence band top were −4.92, −5.32, and −4.73 eV for SP-MMO, SP-MFO, and SP-MCO, respectively. They discussed how the oxidative decomposition of the solvent occurs when the HOMO of the solvent exceeds the top of the valence band. This discussion also explained the experimental results on the order of the oxidative decomposition reaction. However, our calculated results did not support their interpretation of the experiments. As discussed, the HOMO level of the solvent should be lower than that at the top of the valence band.

Quite recently, Zhou et al. reported that theoretical simulations on the 1,2-dimethoxyethane (DME) decomposition on Mg-SP surface.[30] They considered the C–O bond dissociation of DME and concluded that the decomposition reaction is mainly catalytic chemistry rather than the oxidative decomposition. They also performed the decomposition calculations on the Mg-extracted SP surfaces. According to several experiments for Mg-SP, the RS phases are formed on the Mg-SP surface,[33,47] indicating that the Mg deficient SP surface is hard to be realized. Moreover, the decompositions are endothermic even on the Mg-deficient SP surfaces. On the other hand, we also explained the Cut-2 reactions on RS are endothermic. For the SP surfaces covered by RS phases, however, there are M^{3+} ions in the bulk region of SP, which can be reduced by the Cut-2 reaction. We can expect that the Cut-2 reactions on the SP surfaces covered by the RS phase can proceed, if the SP phases are not perfectly transformed into RS phases. Therefore, the observed reactions by Han et al. are presumed to be the Cut-2 reaction.

4. Summary

In this study, we investigated the ether solvent decomposition on MgM_2O_4 (M = Mn, Fe, Co) SP and $MgMO_2$ (M = Mn, Fe, Co) RS surfaces using first-principles calculations. The energetics and changes in the electronic structures of the C–O and C–H bond dissociations on both SP spinel and rock-salt surfaces were examined. We found that the C–H bond dissociation of ether

molecules on the spinel surface was exothermic, irrespective of the transition metal element, whereas other reactions were endothermic. The calculated PDOS for pristine molecule adsorption shows that direct oxidation of the adsorbate is not feasible. The products resulting from the C–H dissociation reactions at the spinel surfaces occupied states originating from the SP surfaces within the bandgap. Because the hydrogen atom behaves as a proton, as revealed by the Bader charge analysis, the spinel oxide surface is effectively reduced, and the corresponding states can be observed inside the band gap in the PDOS. The appearance of occupied states inside the bandgap indicates that the oxidized states should be stabilized. As the spinel surface is destabilized by C–H dissociation, the electrons at this level can be extracted as an oxidative current.

Acknowledgments

The authors thank Dr. Yoshitaka Tateyama and Dr. Tomonobu Nakayama for their fruitful discussions. The calculations were performed using the Numerical Materials Simulator at NIMS and the ITO supercomputer at the Research Institute for Information Technology, Kyushu University. This study was partially supported by JST ALCA-SPRING Grant No. JPMJAL1301, Japan.

CRediT Authorship Contribution Statement

Tomoaki Kaneko: Conceptualization (Equal), Formal analysis (Lead), Investigation (Lead), Writing – original draft (Lead)
Yui Fujihara: Formal analysis (Supporting), Investigation (Supporting), Resources (Lead)
Toshihiko Mandai: Supervision (Supporting), Writing – original draft (Supporting)
Hiroaki Kobayashi: Conceptualization (Equal), Project administration (Equal), Supervision (Equal)
Keitaro Sodeyama: Conceptualization (Lead), Project administration (Lead), Supervision (Lead)

Data Availability Statement

The data that support the findings of this study are openly available under the terms of the designated Creative Commons License in J-STAGE Data listed in D1 of References.

Conflict of Interest

The authors declare no conflict of interest in the manuscript.

Funding

Japan Science and Technology Agency: JPMJAL1301

References

D1. T. Kaneko, Y. Fujihara, T. Mandai, H. Kobayashi, and K. Sodeyama, *J-STAGE Data*, https://doi.org/10.50892/data.electrochemistry.24980718, (2024).
1. K. Shimokawa and T. Ichitsubo, *Curr. Opin. Electrochem.*, **21**, 93 (2020).
2. I. D. Johnson, B. J. Ingram, and J. Cabana, *ACS Energy Lett.*, **6**, 1892 (2021).
3. S. Okamoto, T. Ichitsubo, T. Kawaguchi, Y. Kumagai, F. Oba, S. Yagi, K. Shimokawa, N. Goto, T. Doi, and E. Matsubara, *Adv. Sci.*, **2**, 1500072 (2015).
4. T. Mandai, K. Tatesaka, K. Soh, H. Masu, A. Choudhary, Y. Tateyama, R. Ise, H. Imai, T. Takeguchi, and K. Kanamura, *Phys. Chem. Chem. Phys.*, **21**, 12100 (2019).
5. J. Han, S. Yagi, and T. Ichitsubo, *J. Power Sources*, **435**, 226822 (2019).
6. J. Han, S. Yagi, H. Takeuchi, M. Nakayama, and T. Ichitsubo, *J. Mater. Chem. A*, **9**, 26401 (2021).
7. K. Leung, *J. Phys. Chem. C*, **116**, 9852 (2012).
8. N. Kumar, K. Leung, and D. J. Siegel, *J. Electrochem. Soc.*, **161**, E3059 (2014).
9. K. Leung, *Chem. Mater.*, **29**, 2550 (2017).
10. K. Leung, Rosy, and M. Noked, *J. Chem. Phys.*, **151**, 234713 (2019).
11. Y. Okuno, K. Ushirogata, K. Sodeyama, G. Shukri, and Y. Tateyama, *J. Phys. Chem. C*, **123**, 2267 (2019).
12. J. L. Tebbe, T. F. Fuerst, and C. B. Musgrave, *ACS Appl. Mater. Interfaces*, **8**, 26664 (2016).
13. S. Xu, G. Luo, R. Jacobs, S. Fang, M. K. Mahanthappa, R. J. Hamers, and D. Morgan, *ACS Appl. Mater. Interfaces*, **9**, 20545 (2017).
14. Y. Yu, P. Karayaylali, Y. Katayama, L. Giordano, M. Gauthier, F. Maglia, R. Jung, I. Lund, and Y. Shao-Horn, *J. Phys. Chem. C*, **122**, 27368 (2018).
15. X. Qin, P. B. Balbuena, and M. Shao, *J. Phys. Chem. C*, **123**, 14449 (2019).
16. M. Lin, X. Yang, X. Zheng, J. Zheng, J. Cheng, and Y. Yang, *J. Electrochem. Soc.*, **168**, 050505 (2021).
17. G. Shukri, B. Rendy, A. G. Saputro, F. V. Panjaitan, P. S. Tarabunga, M. K. Agusta, N. N. Mobarak, and H. K. Dipojono, *J. Phys. Chem. C*, **126**, 2151 (2022).
18. M. R. Fuhst and D. J. Siegel, *J. Phys. Chem. C*, **124**, 24097 (2020).
19. X. Sun, R. Xiao, X. Yu, and H. Li, *Langmuir*, **37**, 5252 (2021).
20. Q. Chen, Y. Pei, H. Chen, Y. Song, L. Zhen, C.-Y. Xu, P. Xiao, and G. Henkelman, *Nat. Commun.*, **11**, 3411 (2020).
21. A. Bhandari, J. Bhattacharya, and R. G. S. Pala, *J. Phys. Chem. C*, **124**, 9170 (2020).
22. R. Tatara, Y. Yu, P. Karayaylali, A. K. Chan, Y. Zhang, R. Jung, F. Maglia, L. Giordano, and Y. Shao-Horn, *ACS Appl. Mater. Interfaces*, **11**, 34973 (2019).
23. T. M. Østergaard, L. Giordano, I. E. Castelli, F. Maglia, B. K. Antonopoulos, Y. Shao-Horn, and J. Rossmeisl, *J. Phys. Chem. C*, **122**, 10442 (2018).
24. L. Giordano, P. Karayaylali, Y. Yu, Y. Katayama, F. Maglia, S. Lux, and Y. Shao-Horn, *J. Phys. Chem. Lett.*, **8**, 3881 (2017).
25. M. Gauthier, P. Karayaylali, L. Giordano, S. Feng, S. F. Lux, F. Maglia, P. Lamp, and Y. Shao-Horn, *J. Electrochem. Soc.*, **165**, A1377 (2018).
26. E. G. Leggesse, K.-H. Tsau, Y.-T. Liu, S. Nachimuthu, and J.-C. Jiang, *Electrochim. Acta*, **210**, 61 (2016).
27. L. Giordano, T. M. Østergaard, S. Muy, Y. Yu, N. Charles, S. Kim, Y. Zhang, F. Maglia, R. Jung, I. Lund, J. Rossmeisl, and Y. Shao-Horn, *Chem. Mater.*, **31**, 5464 (2019).
28. L. Huai, Z. Chen, and J. Li, *ACS Appl. Mater. Interfaces*, **9**, 36377 (2017).
29. K. Leung, *Chem. Mater.*, **35**, 2518 (2023).
30. W. Zhou, C. Xu, B. Gao, M. Nakayama, S. Yagi, and Y. Tateyama, *ACS Energy Lett.*, **8**, 4113 (2023).
31. Z. Feng, X. Chen, T. T. Fister, M. J. Bedzyk, and P. Fenter, *J. Appl. Phys.*, **120**, 015307 (2016).
32. S. M. Antao, I. Hassan, and J. B. Parise, *Am. Mineral.*, **90**, 219 (2005).
33. Q. D. Truong, M. K. Devaraju, P. D. Tran, Y. Gambe, K. Nayuki, Y. Sasaki, and I. Honma, *Chem. Mater.*, **29**, 6245 (2017).
34. P. Giannozzi, O. Andreussi, T. Brumme, O. Bunau, M. Buongiorno Nardelli, M. Calandra, R. Car, C. Cavazzoni, D. Ceresoli, M. Cococcioni, N. Colonna, I. Carnimeo, A. Dal Corso, S. de Gironcoli, P. Delugas, R. A. DiStasio, Jr., A. Ferretti, A. Floris, G. Fratesi, G. Fugallo, R. Gebauer, U. Gerstmann, F. Giustino, T. Gorni, J. Jia, M. Kawamura, H.-Y. Ko, A. Kokalj, E. Küçükbenli, M. Lazzeri, M. Marsili, N. Marzari, F. Mauri, N. L. Nguyen, H.-V. Nguyen, A. Otero de-la Roza, L. Paulatto, S. Poncé, D. Rocca, R. Sabatini, B. Santra, M. Schlipf, A. P. Seitsonen, A. Smogunov, I. Timrov, T. Thonhauser, P. Umari, N. Vast, X. Wu, and S. Baroni, *J. Phys.: Condens. Matter*, **29**, 465901 (2017).
35. J. P. Perdew, K. Burke, and M. Ernzerhof, *Phys. Rev. Lett.*, **78**, 1396 (1997).
36. D. Vanderbilt, *Phys. Rev. B*, **41**, 7892 (1990).
37. K. F. Garrity, J. W. Bennett, K. M. Rabe, and D. Vanderbilt, *Comput. Mater. Sci.*, **81**, 446 (2014).
38. S. Grimme, J. Antony, S. Ehrlich, and H. Krieg, *J. Chem. Phys.*, **132**, 154104 (2010).
39. M. Cococcioni and S. de Gironcoli, *Phys. Rev. B*, **71**, 035105 (2005).
40. T. Kaneko, Y. Fujihara, H. Kobayashi, and K. Sodeyama, *Appl. Surf. Sci.*, **613**, 156065 (2023).
41. W. Jin, G. Yin, Z. Wang, and Y. Q. Fu, *Appl. Surf. Sci.*, **385**, 72 (2016).
42. M. Otani and O. Sugino, *Phys. Rev. B*, **73**, 115407 (2006).
43. G. Henkelman, A. Arnaldsson, and H. Jónsson, *Comput. Mater. Sci.*, **36**, 354 (2006).
44. W. Tang, E. Sanville, and G. Henkelman, *J. Phys.: Condens. Matter*, **21**, 084204 (2009).
45. M. Yu and D. R. Trinkle, *J. Chem. Phys.*, **134**, 064111 (2011).
46. E. Sanville, S. D. Kenny, R. Smith, and G. Henkelman, *J. Comput. Chem.*, **28**, 899 (2007).
47. N. L. Okamoto, K. Shimokawa, H. Tanimura, and T. Ichitsubo, *Scr. Mater.*, **167**, 26 (2019).